Geophysical Research Letters

Supporting Information for "Bi-directional Energy Cascades in the Pacific Ocean from Equator to Subarctic Gyre"

Bo Qiu[1], Toshiya Nakano[2], Shuiming Chen[1], Patrice Klein[3,4]

[1]Department of Oceanography, University of Hawaii at Manoa, Honolulu, Hawaii, USA
[2]Atmosphere and Ocean Department, Japan Meteorological Agency, Tokyo, Japan
[3]Environmental Science & Engineering, California Institute of Technology, Pasadena, CA, USA
[4]Jet Propulsion Laboratory, California Institute of Technology, Pasadena, CA, USA

Contents of this file

A. ADCP Data Processing & Statistical Properties

Japan Meteorological Agency utilizes two research vessels, *Ryofu Maru* and *Keifu Maru*, for its repeat hydrographic and shipboard ADCP surveys along 165°E. Hull-mounted 75 kHz broadband ADCPs from Teledyne RD Instruments were used prior to spring 2010 and they were switched to 38 kHz Ocean Surveyor ADCPs thereafter. A total of 38 transects from the period of 2004 to 2020 are selected and analyzed in this study (see Fig.1b). The raw shipboard ADCP data are processed using the Common Ocean Data Access System available from http://currents.soest.hawaii.edu.

Before calculating the 2nd- and 3rd-order structure function (SF), we removed the long-term time-mean velocity to retain the time-varying cross-track and along-track velocities u'_T and u'_L only. This removal of time-mean circulation is a common

practice in velocity SF analyses in related fields; for example, Cho & Lindborg (2001) for aircraft-measured atmospheric winds and Young & Read (2017) for space-aircraft-measured Jupiter atmospheric winds. The objective is to make the u'_T and u'_L field isotropic, a condition required by the SF analysis. To test whether the ADCP-measured velocity fields satisfy the isotropic condition, we show in the left column of Figure S1 the scatter plot of u'_T versus u'_L and calculate their correlation coefficient *R* in the 5 dynamic bands of our interest. As indicated above each panel, the R value falls between –0.053 to 0.121, indicating the isotropic condition is largely satisfied.

A question related to the afore-mentioned isotropic assumption is whether the observed u'_T and u'_L are Gaussian random variables. To address this question, we plot their probability density functions (pdf's) by black lines in the right column of Figure S1. Red lines in each panel shows the best-fit normal distribution. Even though the rms velocity variability is substantially different among the 5 bands, their respective pdf's seem to follow the Gaussian distribution reasonably well. This result is in agreement with the findings by Gille & Llewellyn Smith (2000) based on along-track T/P SSH data; specifically, unless one mixes regions of different underlying dynamics, the velocity pdf would conform to Gaussian distribution.

In our SF analyses, the maximum separation distance is set at $r = 500$km. With the research vessel cruising at ~5 m/sec, this distance can be covered within ~1.2 days. For subinertial balanced motions, we may regard their signals to be "instantaneous" for $r < 500$km. The shortest period for prominent unbalanced motions (like tides, near-inertial oscillations, etc.) is 12 hours. In 12 hours, the research vessel can traverse 216km. For $r > 200$km, there is thus a possibility of aliasing by unbalanced motions on the SF evaluations. As shown by the dashed blue and red lines in the left panel of Figure 3, divergent motions with $r > 200$km is at least 5-folds smaller than the balanced motions. As such, we expect that the aliasing by divergent motions on the SF results shown in Figure 3 would not be that significant. For more quantitative assessment, however, future studies based on model simulation output is called for.

B. Background Circulation along 165°E

Due to the complex basin geometry and external wind/buoyancy forcings, the large-scale upper ocean circulation and its associated variability are spatially, highly inhomogeneous. The JMA section along 165°E is no exception. As depicted in Fig.1a, the time-mean circulation along this section can be broadly divided into five bands with similar governing dynamics and turbulent flow characteristics. The northern band between 40°-50°N is where the wind-driven Western Subarctic Gyre (WSG) is located. As shown in Fig.2a, there exist multiple eastward zonal-mean flows with speed of O(0.1 m/sec) and they represent return flows associated with the wind-forced, subarctic Sverdrup circulation (Favorite et al. 1976; Nakano et al. 2018). Mesoscale eddy variability in this band is the lowest among the five bands along the 165°E section (Fig.2b).

The 30°-40°N band is occupied by the Kuroshio Extension system. Due to the presence of Shatsky Rise to the immediate west of 165°E, the downstream Kuroshio Extension jet observed in Fig.2a is split into multiple eastward jets and adjacent recirculating flows. In this band, mesoscale eddy variability has the highest level along 165°E as a result of the intrinsically unstable Kuroshio Extension system (Qiu and Chen 2005; Waterman et al. 2011; Yang and Liang 2016).

The 17°-30°N band across the center of the wind-driven subtropical gyre sees the presence of multiple surface-trapped eastward jets, known as the Subtropical Countercurrents (STCCs). Within this band, enhanced mesoscale eddy variability is generated by baroclinic instability of the vertically-sheared, eastward STCC in the surface layer and westward North Equatorial Current (NEC) in the subsurface layer (Qiu 1999; Kobashi and Kawamura 2002). Compared to the Kuroshio Extension, eddy activity in the STCC band is weaker and is confined to the 200m upper ocean (Fig.2b).

The westward NEC in the 7°-17°N band represents the return flows of the interior Sverdrup transport for the wind-driven North Pacific tropical and subtropical gyres (Fig.2a). Despite being an intense zonal current, the NEC is relatively stable and this dynamical stability is related to the lack of change in meridional gradient of potential vorticity in its mean flow structure (Qiu 1999; Tulloch et al. 2011).

The equatorial band between 5°S-7°N is occupied by a series of zonal flows. In the surface 300m layer, the westward South Equatorial Current exists south of the equator, the eastward North Equatorial Countercurrent (NECC) appears north of 1°N, and the eastward Equatorial Undercurrent (EUC) straddles the equator in the 100-300m layer. These time-mean surface current systems are mostly wind-driven, but unlike the Kuroshio Extension and the STCCs in the subtropical gyre whose variability is dominated by baroclinic instability, the eddy variability in the equatorial band is driven largely by barotropic instability that results from lateral shears of the time-mean zonal flows (Philander 1976; Chen et al. 2015).

Supporting References

Chen, X., Qiu, B., Chen, S., Qi, Y. & Du, Y. (2015). Seasonal eddy kinetic energy modulations along the North Equatorial Countercurrent in the western Pacific. *J. Geophys. Res.*, **120**, 6351-6362.

Cho, J.Y.N. & Lindborg, E. (2001). Horizontal velocity structure functions in the upper troposphere and lower stratosphere: 1. Observations. J. Geophys. Res., 106, 10223-10232.

Favorite, F., Dodimead, A. & Nasu, K. (1976). Oceanography of the subarctic Pacific region, 1960-1971. *Bull. Int. North Pacific Fish. Comm*. **33**, 1-187.

Gille, S.T. & Llewellyn-Smith, S.G. (2000). Velocity probability density functions from altimetry. J. Phys. Oceanogr., 30, 125-136.

Kobashi, F. & Kawamura, H. (2002). Seasonal variation and instability nature of the North Pacific Subtropical Countercurrent and the Hawaiian Lee Countercurrent. *J. Geophys. Res*., **107**, C03185.

Nakano, H., Tsujino, H., Sakamoto, K., Urakawa, S., Toyoda, T. & Yamanaka G. (2018). Identification of the fronts from the Kuroshio Extension to the Subarctic Current using absolute dynamic topographies in satellite altimetry products. *J. Oceanogr.*, **74**, 393-420.

Philander, S. (1976). Instabilities of zonal equatorial currents. *J. Geophys. Res*., **81**, 3725-3735.

Qiu, B. (1999). Seasonal eddy field modulation of the North Pacific Subtropical Countercurrent: TOPEX/Poseidon observations and theory. *J. Phys. Oceanogr*., **29**, 2471-2486.

Qiu B. & Chen S. (2005). Variability of the Kuroshio Extension jet, recirculation gyre, and mesoscale eddies on decadal time series. *J. Phys. Oceanogr*., **35**, 2090-2103.

Tulloch, R., Marshall, J., Hill, C. & Smith, S.S. (2011). Scales, growth rates, and spectral fluxes of baroclinic instability in the ocean. *J. Phys. Oceanogr*., **41**, 1057-1076.

Waterman, S., Hogg, N., & Jayne, S. (2011). Eddy-mean flow interaction in the Kuroshio Extension region. *J. Phys. Oceanogr*., **41**, 1182-1208.

Yang, Y. & Liang, X. (2016). The Instabilities and multiscale energetics underlying the mean-interannual-eddy interactions in the Kuroshio Extension Region. *J. Phys. Oceanogr*. **46**, 1477-1494.

Young, R.M.B., & Read, P.L. (2017). Forward and inverse kinetic energy cascades in Jupiter's turbulent weather layer. Nat. Physics, 13, DOI: 10.1038/NPHYS4227.

Supporting Figure

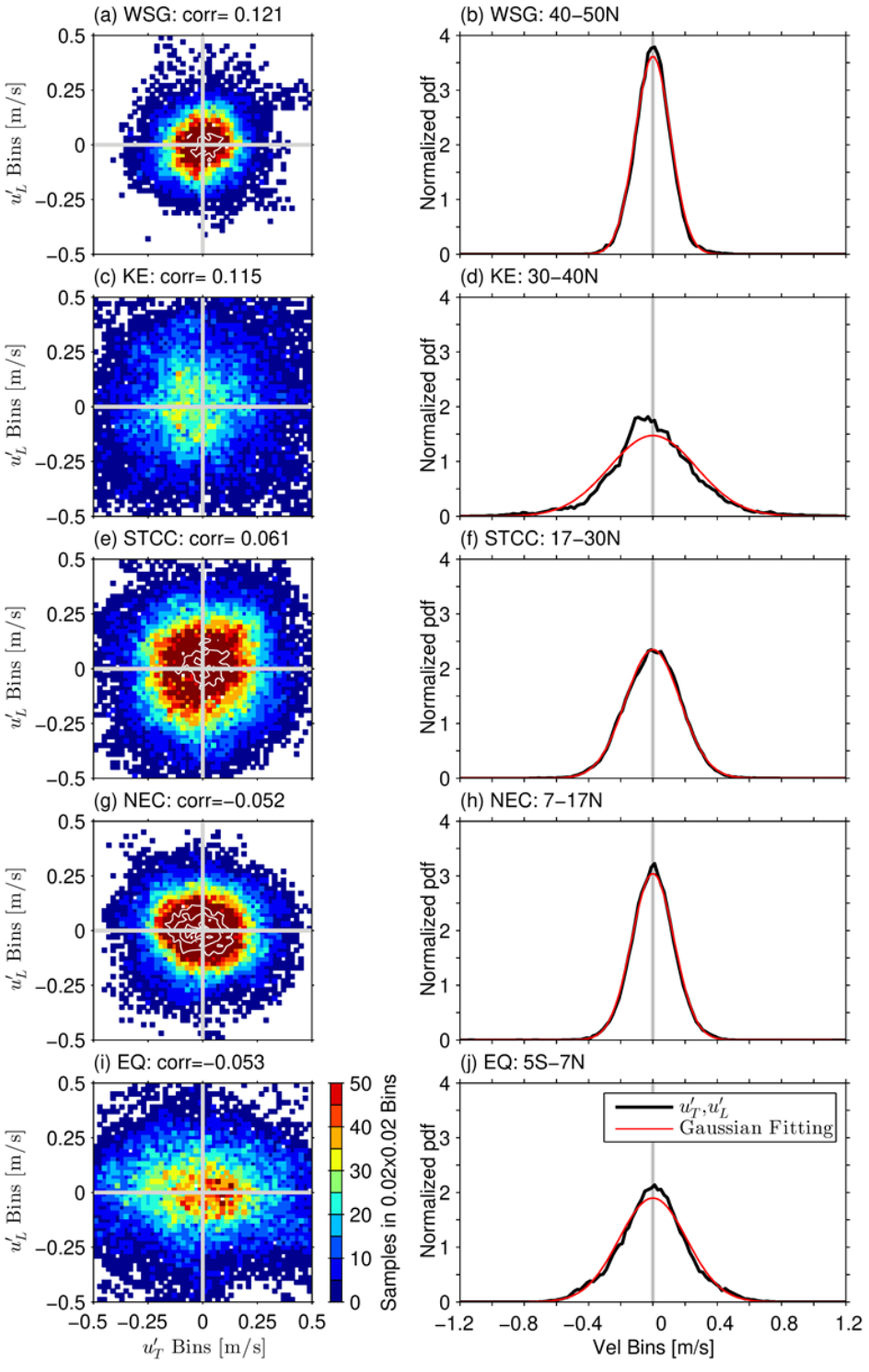

Figure S1: Left column: Scatter plot of u'_T and u'_L observed in the bands of (a) WSG, (c) Kuroshio Extension, (e) STCC, (g) NEC, and (i) Equator. Linear correlation coefficient between u'_T and u'_L in each band is indicated above each plot. Right column: Probability density function distributions (black lines) in the corresponding five bands. Red lines indicate the best-fits to a Gaussian, or normal, distribution.